



Investigating the controlled microstructure features and the corrosion performance of laser beam powder bed fused Ti6Al4V alloy

Tohid Rajabi¹ · Hamid Reza Ghorbani¹ · Masoud Atapour¹ · Ozkan Gokcekaya² · Takayoshi Nakano²

Received: 7 April 2024 / Accepted: 12 August 2024
© The Author(s), under exclusive licence to Springer Nature Switzerland AG 2024

Abstract

Currently, there is a significant level of interest in the use of additive manufacturing (AM) technology for implant applications. The utilization of titanium alloy implants, particularly those employing Ti6Al4V produced via powder bed fusion using a laser beam (PBF-LB), is expected to optimize osteointegration between the implant and the corresponding bone. The corrosion behavior is crucial for such applications and the process parameters of PBF-LB exhibit noteworthy impacts on both microstructure and corrosion behavior. The impact of PBF-LB process parameters, with a particular focus on laser scan strategy and hatch space, on the microstructure control and corrosion properties of Ti6Al4V remains to be comprehensively studied. Therefore, a comparative analysis was carried out to evaluate the efficacy of two laser scanning strategies, namely X scan and XY scan with two different volumetric energy densities (VED). Results showed that martensitic microstructure formed in both samples due to the fast-cooling speed of the PBF-LB process. Moreover, the EBSD results indicated the remelting effect on grain structure in XY and XZ observation planes. Corrosion investigations revealed that the optimum corrosion behavior of the PBF-LB specimens was obtained from the XY plane of the XY scan strategy. The findings of this study indicate that a controlled microstructure approach via simultaneous change of laser scanning strategy and hatch space can effectively modify the microstructure and corrosion characteristics of Ti6Al4V alloy.

Keywords Laser beam powder bed fusion · Scan strategy · Ti6Al4V · Corrosion · Microstructure

1 Introduction

Additive Manufacturing (AM), considered a game-changing technology and a key component of Industry 4.0, holds immense promise in revolutionizing production methods across diverse fields and industries. Its applications span from space exploration beyond Earth's boundaries to medical advancements within the human body, such as the fabrication of high-quality, customized implants for hard tissue replacement. AM processes enable the precise fabrication of complex solid objects, including intricate geometries,

by building them layer by layer using sliced CAD models [1]. Currently, there are several applications in the field of dentistry that allow for the production of patient-specific devices for dental and maxillofacial rehabilitation [2]. Additionally, the implementation of Powder-Based Fusion (PBF) technologies has the potential to facilitate the production of cobalt-chromium (Co-Cr) and titanium (Ti) metal frameworks. These frameworks are utilized in the fabrication of removable partial dentures (RPDs) and fixed dental prostheses, which can be supported by either natural teeth or dental implants [3, 4].

Nowadays, AM of metallic components (including single or multi-materials [5]) has gained significant interest in both academic and industrial terms. For instance, some titanium alloys (CP-Ti, Ti6Al4V [6, 7]), steels [8], CoCrMo [9], and tungsten [10], were fabricated by AM technology. Among these materials, additive manufacturing of titanium alloys has garnered considerable attention due to the combination of unique properties offered by titanium alloys and the special capabilities of additive manufacturing [11].

✉ Hamid Reza Ghorbani
hr.ghorbani@ma.iut.ac.ir

✉ Masoud Atapour
m.atapour@cc.iut.ac.ir

¹ Department of Materials Engineering, Isfahan University of Technology, Isfahan 84156-83111, Iran

² Division of Materials and Manufacturing Science, Graduate School of Engineering, Osaka University, Osaka 565-0871, Japan

Titanium-based alloys have remarkable properties such as low density, superior biocompatibility, low modulus of elasticity, high specific strength, good mechanical properties, and good corrosion resistance. Ti6Al4V alloy is one of the most widely used titanium alloys for industrial and medical purposes. Recently, there has been a growing interest in producing Ti alloys, especially Ti6Al4V, with customized properties for specific applications. Additive manufacturing has shown significant progress in producing titanium alloys with complex or porous geometries that have unique properties [11]. For instance, the Ti6Al4V alloy has been additively manufactured for dental implants with a porous scaffold structure that improved osseointegration, fixation, and stability of the implant [12]. Kim et al. [13] also reported that the optimized additively manufactured Ti6Al4V specimens had similar biological properties to the machine-cut ones, suggesting the potential use of AM in various dental applications such as customized dental implants and implantable prosthodontics [13]. Furthermore, AMed Ti6Al4V has been explored for applications such as single and double-root implants [14], scaffolds for bone repair [15], and large customized devices for restoring dental function, supporting implants, and promoting bone regeneration [16]. Recently, grooved-structured Ti alloy fabricated by AM has been proven to align cell growth direction while exhibiting an inhibitory effect on bacteria adhesion [17]. AM is becoming popular in healthcare because of its ability to produce precise and accurate patient-specific implants [18]. Moreover, AM can produce dental parts at a much lower cost and in less time than subtractive manufacturing techniques [19]. However, more aspects of AMed Ti6Al4V alloy need to be studied, such as different AM methods and the effects of build strategies and process parameters on the properties and corrosion resistance for dental applications.

Different AM [20] and hybrid additive manufacturing (HAM) [21, 22] methods have been used to produce Ti6Al4V samples, such as Laser Powder Bed Fusion (PBF-LB), also known as Selective Laser Melting (SLM) [23, 24] and Electron Beam Powder Bed Fusion (PBF-EB) [21, 25]. PBF-LB can produce fully dense customized metal parts with superior mechanical properties and offers a time-efficient and energy-efficient approach [19, 26]. In particular, PBF-LB can produce complex components using titanium alloys, which are widely used in biomedical settings [19]. However, PBF-LB has some features that need to be considered, such as a very high-temperature gradient (10^6 K/m), high cooling rate (up to 10^8 K/s), rapid solidification, and complex heat history including melting, solidification, several reheating and cooling cycles. These features result in a microstructure of PBF-LBed Ti6Al4V alloy that consists of columnar prior β grains and fine α' martensite phases (hierarchical structure) with a high density of dislocations and twins [20, 27]. PBF-LBed Ti6Al4V parts

usually undergo heat treatment to transform martensitic α' to α and reduce stress concentration [26].

The properties of materials (such as electrochemical, biological, mechanical, and physical properties) are greatly affected by their microstructures, which include phase composition, morphology, and distribution. These microstructural features depend on the processing techniques and conditions used during fabrication [27]. To achieve optimized microstructure in PBF-LB, a suitable combination of laser beam parameters is needed, which influence the temperature distribution, the melt pool formation, and the heat transfer mechanism. These parameters include scan strategy, power (P), powder layer thickness (h), laser hatch spacing (d), and scanning speed (v) [28]. The challenge is to optimize the PBF-LB parameters to obtain the desired controlled microstructure and consequently better electrochemical behavior for dental applications.

Yang et al. [27] studied the martensite formation in PBF-LBed Ti6Al4V and found that the martensite size can be controlled by processing parameters such as hatch spacing and scan velocity. For example, the martensite size increased with hatch spacing. Also, the martensite size first increased and then decreased by increasing the scan velocity. They also discussed the formation and control of the α' martensite (including primary, secondary, ternary, and quartic) and its relation to heat history in the PBF-LB process [27]. Barba et al. [26] conducted a comprehensive study and found that the AM process and sample size strongly affected the α -lath and prior- β grain sizes. They also found that by increasing the laser energy density, the prior- β grain width increased and the α' martensite size decreased. Moreover, a strong β solidification texture was achieved due to the partial remelting of solidified layers. Furthermore, the laser scanning speed and scan strategy affected the thermal flux direction, which in turn affected the β grain growth direction [29]. Simonelli et al. [30] investigated the texture formation during the PBF-LB process and found that solidification texture and hence the final microstructure development can be strongly influenced by the rotating scan strategy. In another work, the porosity level of the PBF-LBed Ti6Al4V was reduced by increasing the laser power and/or decreasing the scan speed and hatch spacing [31].

The corrosion behavior of the Ti6Al4V alloy has been examined in various solutions to better understand its performance in different applications. The corrosion of titanium alloys is a critical factor in medical treatments [32, 33]. Despite the superior corrosion properties of Ti6Al4V alloy in the biological media, the manufacturing process affects its electrochemical behavior. Xiang et al. [34] declared that the best corrosion performance of the PBF-LBed Ti6Al4V alloy was obtained with 1100 mm/s scanning speed and 280 W laser power. Moreover, better biocompatibility was achieved with 1200 mm/s scanning

speed and 200 W laser power. It was suggested that the effect of scanning speed is stronger than laser power, meanwhile, phases and defect holes were proposed as affecting factors. Leban et al. [35] illustrated that the PBF-LB Ti6Al4V alloy presented higher corrosion resistance as compared with the wrought sample in artificial saliva due to the different microstructure.

Despite numerous publications on the AMed Ti6Al4V alloy, there is still a need to explore and fill the gap in the effects of PBF-LB process parameters to achieve a controlled microstructure and investigate its effect on the properties of Ti6Al4V for specific applications like dental implants. The scan strategy and building direction of PBF-LB have significant effects on the corrosion behavior of PBF-LB parts [36]. Different scan strategies and building directions can create different microstructures, mechanical properties, and surface characteristics that influence the corrosion resistance of PBF-LB parts in various environments. Additionally, hatch space can affect the energy density and subsequently the microstructure of the PBF-LB parts. To achieve a controlled microstructure, it is important to optimize these parameters according to the desired performance and application of PBF-LB parts. Therefore, this research aimed to control the microstructure via the approach of simultaneous change of laser scanning strategy and hatch space (energy density). In this study, two different hatch spaces (low and medium) and two scanning strategies, namely X- and XY-scanning, were employed to provide insights into this matter.

2 Experimental

2.1 Sample fabrication and characterization

Ti6Al4V spherical powder, sourced from EOS in Germany, was utilized as the initial material for this study. The powder exhibited a size distribution characterized by D10, D50, and D90 values of 29.2 μm , 41.2 μm , and 57.4 μm , respectively. Plasma atomization was employed to produce the powder. To determine the particle size distributions (PSD), a Mastersizer 3000E instrument from Malvern Panalytical in the UK was employed. Table 1 provides the chemical composition of the commercial EOS Ti6Al4V powders used in this research. These powders were devoid of any entrapped porosities or satellites, resulting in excellent flowability and packing density (Fig. 1).

An EOS M290 printer with a 400 W Yb-fiber laser was used to fabricate Ti6Al4V. The building plate was preheated to 80 °C to prevent thermal shocks caused by the laser energy input and to ensure consistent fabrication conditions. The building chamber was filled with high-purity argon gas to keep the oxygen content below 100 ppm. A meander scan strategy with scan lines covering the entire 10 \times 10 mm scan area was used to fabricate 10 mm high specimens for microstructure observations. A bidirectional laser scanning was applied in the x-direction only (X-scan) and with a 90° rotation between adjacent layers (XY-scan), as shown in Fig. 2.

Table 1 Composition of the Ti6Al4V powder

Element	Al	V	C	O	Fe	N	H	Ti
Weight (%)	6	4	0.03	0.15	0.1	0.01	0.003	Balance

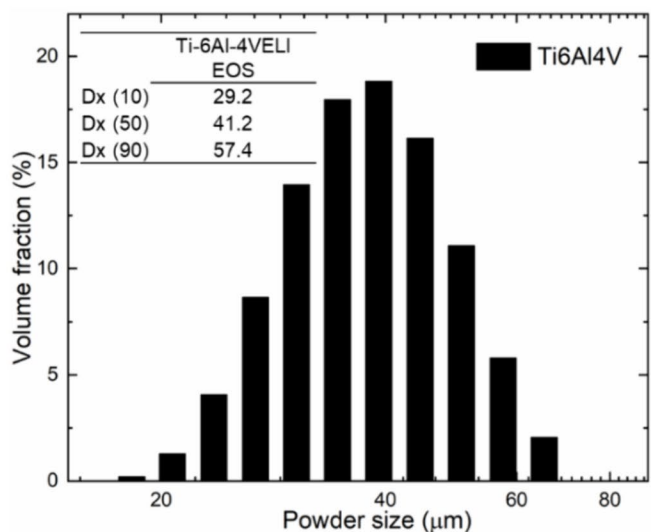
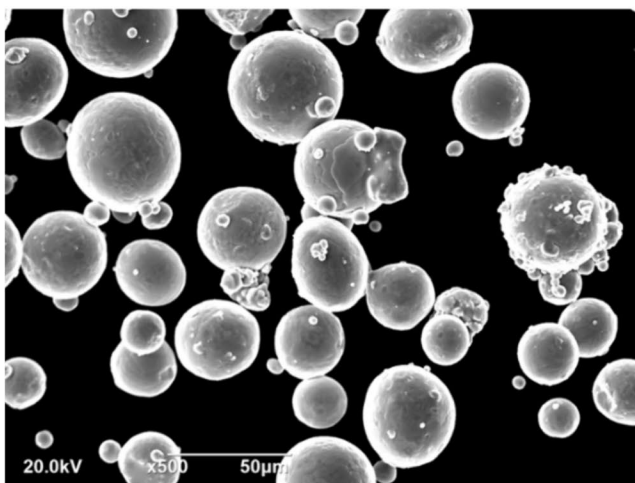


Fig. 1 Powder size distribution of Ti6Al4V powders with a microscope image of the powders

The PBF-LB process parameters for the Ti6Al4V samples were fixed at a layer thickness (t) of 0.060 mm, a laser power (P) of 360 W, and a scan speed (v) of 1200 mm/s. The hatch spacing (h) was varied from 0.030 to 0.100 mm, as listed in Table 2. Three cubic specimens were used per each condition. The volumetric laser energy density (E [J/mm³]) of the fabrication conditions is defined by $E = P/v \cdot t \cdot h$ [37], indicating a high energy density for X scan and a low energy density for XY scan fabrications.

2.2 Solidification calculations

Solidification of the PBF-LB Ti6Al4V alloy has been calculated using Thermo-Calc^R software and the TCTI 4 database. Classic Scheil solidification calculations were configured to start temperature at 5000 °C, capturing the evaporation and calculating the material properties down to room temperature for additive manufacturing of Ti6Al4V alloy. Moreover, a Scheil with solute trapping (ScST) calculation has been done with similar configurations and also by setting the scanning speed to 1.2 m/s and the angle α to 45°. The ScST uses solute trapping in the primary phase for calculations that have a rapid solidification rate such as additive manufacturing applications. The local solidification rate in the Scheil with solute trapping is calculated using the following formula in which V_b is the scanning speed and α is the transformation angle between the melt pool boundary and laser scanning direction (Fig. 3) [38].

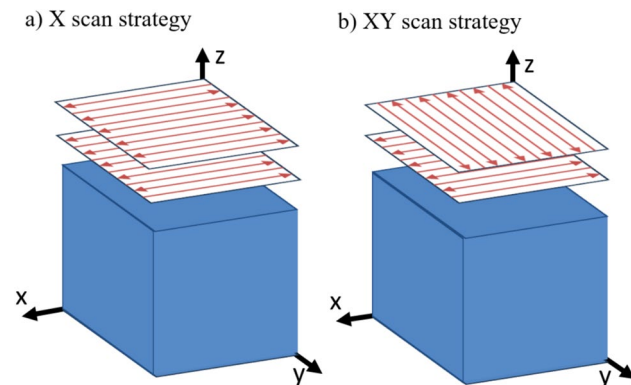


Fig. 2 Scan strategies used for printing samples **a** X scan and **b** XY scan

$$V_s = V_b \cos \alpha.$$

2.3 Surface characterization

The specimens were ground up to 1200 SiC grit paper and chemically etched for 20 s in the Kroll's agent. Then, their microstructure was examined using an optical microscope (Nikon EPIPHOT 300) and a scanning electron microscope (Philips XL30). The microstructural analyses of the Ti6Al4V samples fabricated by PBF-LB with different scan strategies and energy densities aimed to reveal the microstructural differences and their effects on the corrosion and degradation behavior in different biological environments. The microstructural characterization was performed on the XY plane (perpendicular to the build direction (BD)) and the XZ and the YZ plane (parallel to the BD). The cross-sections were mirror-polished and observed by field-emission scanning electron microscopy (FE-SEM; JEOL JIB-4610F, Japan) with an electron backscatter diffraction system (EBSD, NordlysMax3 system, Oxford Instruments, UK, operated at 20 kV accelerating voltage) to identify the microstructural features. Then, the EBSD data were cleaned of non-indexed pixels and visualized using HKL Channel 5 software (Oxford Instruments, UK). From these results, the quantitative analysis of the grain size, grain boundary (GB) misorientation, recrystallization rates, and kernel average misorientation (KAM) were obtained.

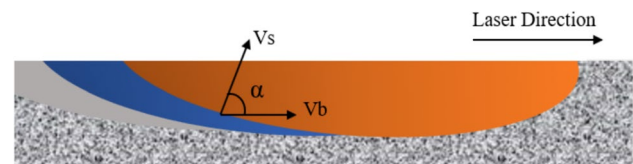


Fig. 3 Schematic of the laser melt pool with the direction of scanning speed and solidification direction angle

Table 2 PBF-LB process parameters of Ti6Al4V samples

	Scan strategy	Laser power (W)	Speed (mm/s)	Hatch (mm)	Thickness (mm)	E (J/mm ³)
Sample-1	X scan	360	1200	0.030	0.06	166.7
Sample-2	XY scan	360	1200	0.100	0.06	50.0

2.4 Electrochemical tests

The corrosion tests were conducted at a temperature of $37 \text{ }^\circ\text{C} \pm 5 \text{ }^\circ\text{C}$ using a three-electrode system. The system consisted of specimens with an exposed area of 10 mm^2 as the working electrode, a platinum mesh as the counter electrode, and an Ag/AgCl saturated KCl electrode as the reference electrode. All corrosion tests were performed using a galvanostat (PARSTAT 2273). Prior to the investigation, all tested samples were abraded using 1200 # SiC grit paper and then cleaned ultrasonically in acetone for 5 min; then, the as-mentioned samples were immersed in both Ringer's solution [pH 6.5] and 0.1 M HCl [pH 1.5] solution at the open circuit potential (OCP) condition for 60 min.

The polarization potentiodynamic test was performed from -250 mV vs. OCP to 1.0 V vs. Ag/AgCl and at a scan rate of 0.32 mV s^{-1} . The electrochemical impedance spectroscopy (EIS) test was conducted in the frequency range of 100 mHz with a current amplitude of 10 mV . Additionally, long-term EIS measurements were executed by immersing the samples in both solutions for a duration of 168 h. Also, it should be mentioned that all the electrochemical tests were repeated at least three times and were performed after 60 min of OCP condition.

3 Results and discussion

3.1 Microstructure evaluations

Figure 4 shows the results of Scheil calculations using two modes, Classic Scheil and Scheil with Solute Trapping (ScST) calculations showing a predicted non-equilibrium solidification following selective laser melting of the Ti6Al4V alloy. As can be seen

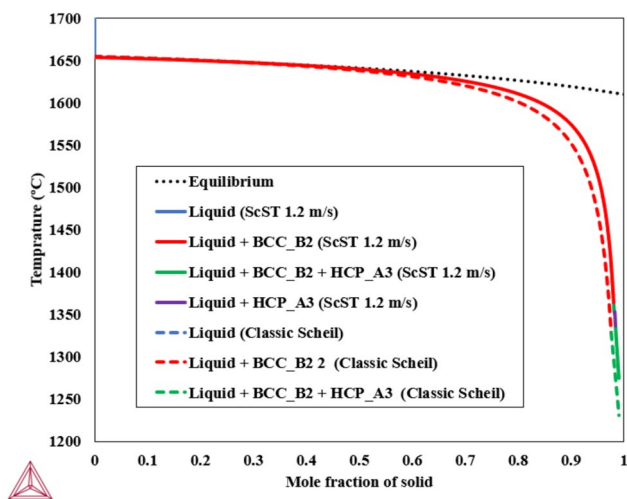


Fig. 4 Results of un-equilibrium solidification calculation using Classic Scheil and Scheil with Solute Trapping (ScST) calculations

from Fig. 4, based on both calculation modes, most of the solidification path goes through the β phase (BCC_B2) and a minor amount of α phase (HCP_A3) has been predicted at the end of the solidification. Further transformation of the phases after solidification till the room temperature has not been calculated, but due to the rapid cooling rate in the PBF-LB process and the relevant literature [29], martensite transformation is expected to be the main transformation for the PBF-LB Ti6Al4V alloy.

Figure 5 depicts 3D illustrations of the optical microscopy (OM) images of the Ti6Al4V alloy produced by PBF-LB via X-scan and XY-scan strategies. As can be seen from Fig. 5, different hatch spaces and scanning strategies resulted in different controlled microstructures and arrangements of the phases. For example, prior β grains and chessboard patterns are clearly seen in XY and XZ planes of the X-scan (Fig. 5a) and XY-scan samples (Fig. 5b), respectively. Additionally, Table 3 presents the percentage of the porosities in the XY and YZ planes of the samples. As it is shown in Table 3, it can be said that those planes have a similar percentage of porosities.

Figure 6 shows optical microscopy micrographs of the microstructure in X-scan and XY-scan samples. The prior β grains, acicular α' martensite, melt pool boundaries, and chessboard pattern are seen in Fig. 6. On the YZ plane of the X scan sample (Fig. 6a''), the wavy-looking lines are the connected melt pool boundaries. However, it is seemingly difficult to observe melt pools on the XY scan sample because it was made by the XY scan strategy, moreover, another reason for undetectable melt pools is the phase transformation during fabrication. Due to β to α phase transformation in Ti6Al4V alloy during solidification, melt pool boundaries are most likely to disappear. Also as shown in Fig. 6, large prior β grains aligned to the build direction (Z) are seen in the microstructure of the XY, XZ, and YZ planes in the X scan sample, however, large prior β grains are only seen in the YZ plane of the XY scan sample due to the scan strategy and formation of the chessboard pattern. As can be seen from Fig. 6, the microstructure of both samples mainly consisted of α' martensite. Interestingly, α' martensite has been formed in various directions and arrangements inner the prior β grains and inner of each chessboard cell, even α' martensite lath shapes like a cross have been detected (Fig. 7). This microstructural feature was related to the prior β grain formation and orientation due to the scan strategy affecting remelting and heat treatment history during melting and solidification of each layer, eventually resulting in differences in $\beta \rightarrow \alpha$ selection during the phase transformation. The hatch space can also be measured in Fig. 7.

Figure 8 shows SEM micrographs of the microstructures in the X-scan and XY-scan samples. Additionally, Table 4, presents the results of EDS analyses showing uniform chemical composition along different samples

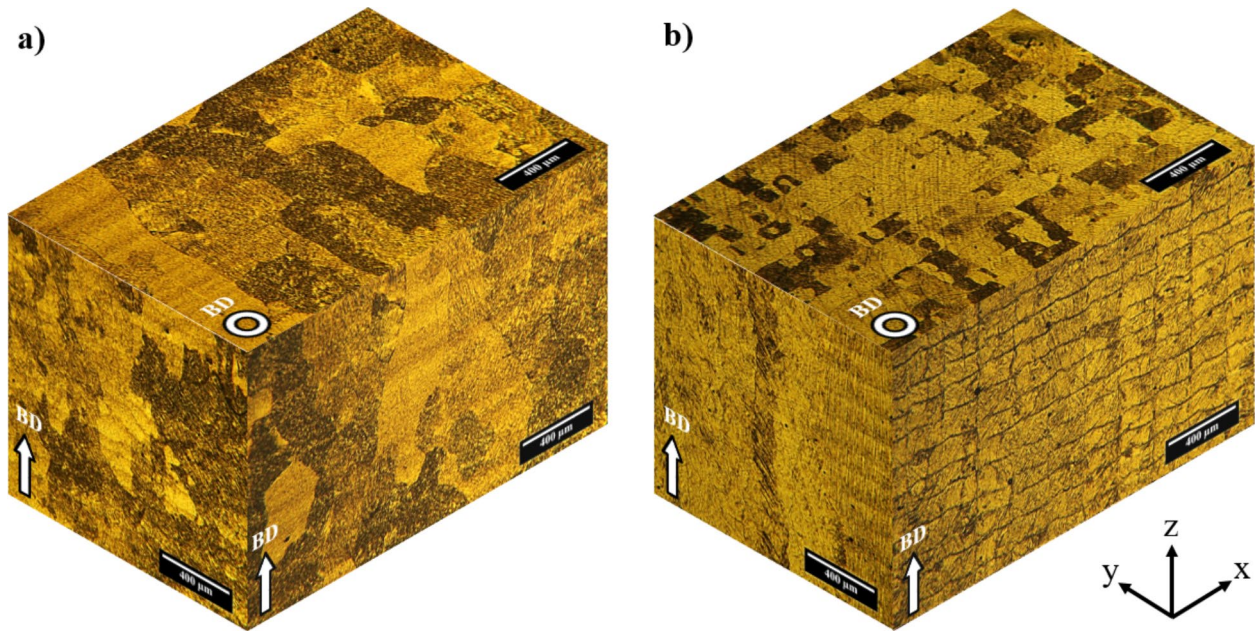


Fig. 5 The 3D illustration of the optical microscopy microstructures in the PBF-LBed Ti6Al4V samples fabricated via **a** X scan and **b** XY scan strategy

Table 3 Porosities percentage of the samples

Samples/Plane	XY	YZ
X scan	0.06 ± 0.01	0.05 ± 0.02
XY scan	0.05 ± 0.02	0.03 ± 0.01

and observation planes, especially in the case of different martensite morphologies. As can be seen from Fig. 8, prior β grain boundaries, acicular α' martensite, and melt pool boundaries were formed in the samples. It seems that plate-like martensite has been formed in the XY plane of the X scan sample and acicular martensite has been formed in the XZ and YZ planes of the X scan sample. Maybe due to the larger cooling rate in the XZ and YZ planes in comparison to the XY plane resulted from different thermal and solidification conditions between those planes [27].

It is worth mentioning that based on the related publications [27, 29], typically a hierarchical martensite structure having a high density of twins and dislocations, including primary, secondary, tertiary, and quartic α' martensite are formed within prior β grains following PBF-LB of Ti6Al4V alloy. Moreover, two different metastable variants of martensite including the HCP α' martensite and orthorhombic α'' martensite have been identified in the work [39]. Therefore, martensite is the main part of the microstructure in the PBF-LBed Ti6Al4V alloy, however, a small amount of α_2 and β have been identified in a few research [27, 29].

The details of microstructure characteristics of X scan and XY scan samples were analyzed by EBSD for the XY plane and YZ plane. Figure 9 represents the IPF maps (a-d), phase maps (a'-d'), and recrystallization maps (a''-d'') of PBF-LBed Ti6Al4V samples observed from the planes perpendicular (XY plane) and parallel (YZ plane) to the build direction. The IPF map of the Ti6Al4V samples did not show the occurrence of any specific α selection, in which each color indicates a grain with a different crystal orientation. Regarding the β phase being the parent phase, the α phase normally precipitates in β matrix, furthermore, α grain precipitation follows the Burgers orientation relationship (BOR): $(0001)\alpha // (110)\beta$, $[11.20]\alpha // [111]\beta$ to form crystallographic anisotropy. Within the BOR, there are 12 variations for α grains to form. Besides, the α variation selection can enhance mechanical properties in an anisotropic manner [40]. However, in this study, the α grains were selected randomly from 12 possible variations from the prior β phase according to Burger orientation relation (BOR) [30] as indicated by the parent β phase, as indicated α phase pole figures (PFs) following BOR. Therefore, it is expected that there is no anisotropy in terms of mechanical properties regarding the α variation selection. Besides, phase maps indicated that the microstructure consisted of a major α phase exhibited acicular α' martensite due to the fast cooling speed of the PBF-LB process [27]. The quantitative analysis of phase fractions showed less than 1% remaining β phase in the microstructure, which was expected to be insignificant for the outcomes of the corrosion results. Additionally, the

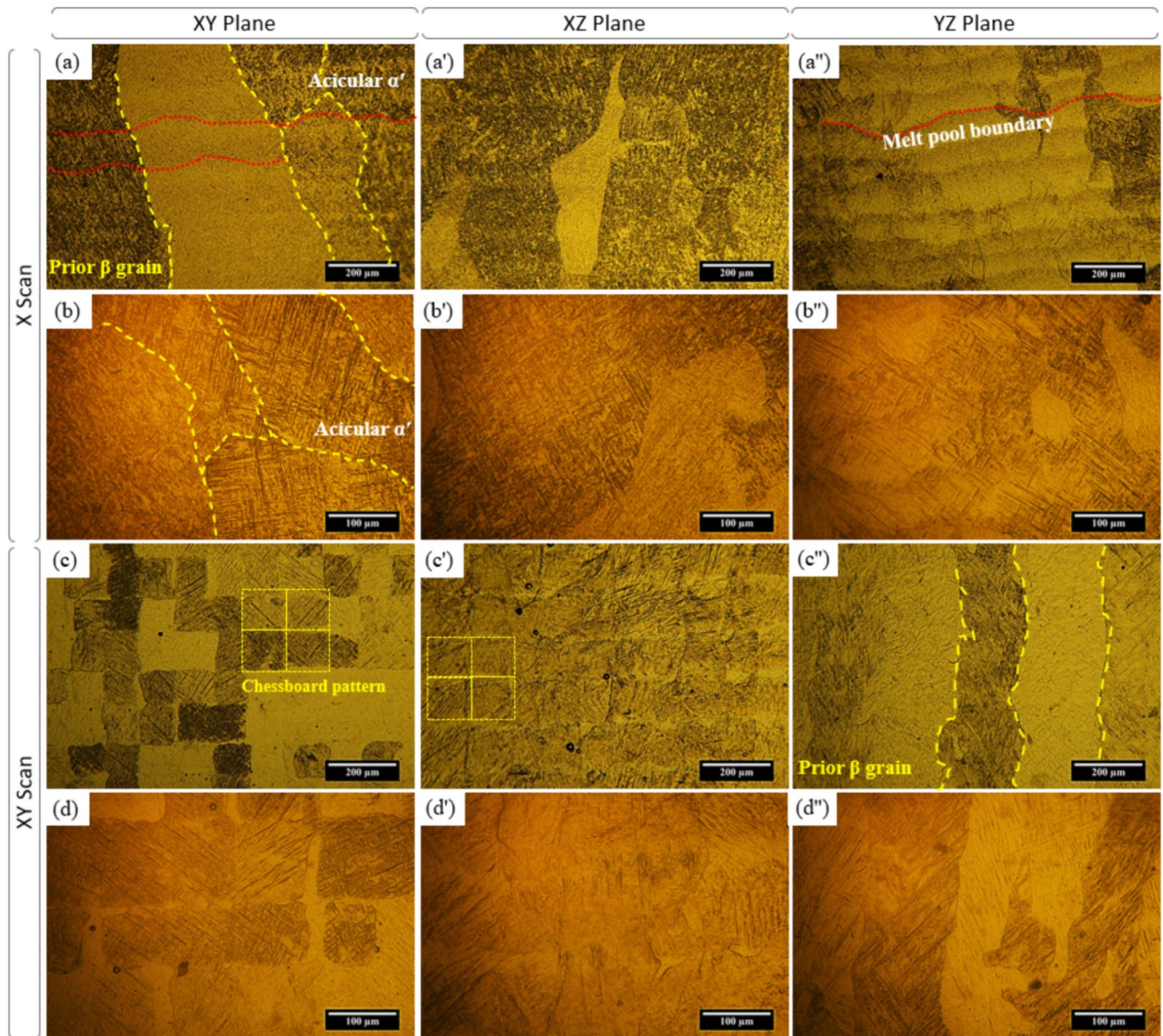


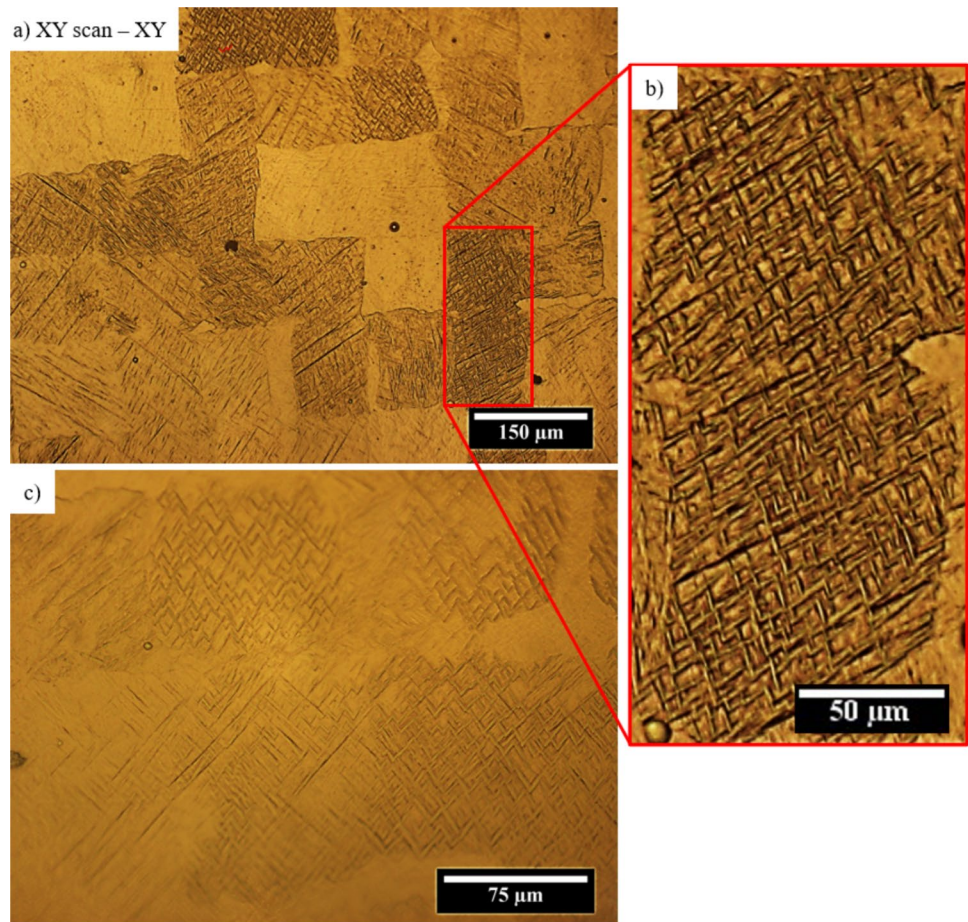
Fig. 6 Optical micrographs of the **a–d** XY plane, **a’–d’** XZ plane and **a’’–d’’** YZ plane of the PBF-LBed Ti6Al4V samples via **a, b** X scan and **c, d** XY scan strategy

difference in grain size of acicular α' martensite depending on scan strategy [41] and/ or laser energy density [28] and the observation plane [26] was qualitatively detected.

The quantitative analyses of the grain size distribution of PBF-LBed Ti6Al4V samples are shown in Fig. 10a regarding the scan strategy and observation plane. The grain size was higher in the YZ plane owing to the epitaxial growth of the prior β phase, promoting columnar grains in multiple layers compared to the XY plane for each sample. The difference regarding average grain sizes of XY and YZ planes for the X-scan and XY-scan differed due to the laser energy input which resulted in the highest and lowest average grain size for X-scanned Ti6Al4V with high laser energy density.

While X-scan with higher energy density was expected to increase remelting and result in a bigger grain size of the prior β phase in the YZ plane and bigger columnar β grains transformed to α phase with the rapid cooling, resulting in bigger grains on the BD (YZ plane). The remelting was less in XY-scan with low energy density, therefore, showing a smaller difference in XY and YZ planes in terms of grain size distribution. The random selection of the α phase from the prior β phase according to BOR exhibited a similar tendency for each sample and each observation plane as indicated by the grain boundary misorientation distribution (Fig. 10b). The difference in the intensity of grain boundary misorientations suggested that the detected number of grains

Fig. 7 The α' martensite in the XY plane of the XY scan sample



varied, thus the fraction of grain boundaries corresponded in a similar manner.

The characteristics of grain structure were quantitatively shown in recrystallization maps and the grains were classified into recrystallized (blue), substructure (yellow), and deformed (red) as shown in Fig. 9a''–d''. The characteristics of grains were related to the controlled microstructure approach including layer-by-layer melting with different laser energy inputs and observation planes with different thermal histories. The quantitative analysis of grain types was demonstrated in Fig. 11a. It has been reported that high energy density formed wider and deeper melt pools while causing large thermal stresses on the grains due to the high volume of remelting, thus, X-scan with high laser energy density composed of a high ratio of deformed grains on XY plane while the high energy input resulted in large heat affected zone (HAZ) with each melting layer and promoted recrystallization on YZ plane (parallel to the BD). A similar tendency of grain characteristics was detected for the XY-scan, however, the difference in XY and YZ planes was less significant compared to the X-scan due to the lower energy input, indicating isotropic microstructural features. The same phenomena can be identified from KAM results

as shown in Fig. 11b. KAM data represents misorientation in grain due to the possible residual stress [42]. The highest KAM value, indicating the highest stress accumulation in grains, was reported for the XY plane of the X-scanned Ti6Al4V sample, which also exhibited the highest rate of deformed grain. Moreover, the difference in KAM values of the X scan for XY and YZ planes was significantly higher compared to the XY scan results. This is a strong indication of the remelting effect on grain structure which depends on the observation plane due to the layer-by-layer fabrication along the BD and the HAZ of different laser energy densities.

3.2 Corrosion investigations

3.2.1 Potentiodynamic polarization

The potentiodynamic polarization curves of the PBF-LBed materials in the Ringer's and diluted HCl solutions at 37 °C are shown in Fig. 12. Also, the results obtained from the potentiodynamic polarization of the aforementioned samples in the Ringer's and diluted HCl solutions are summarized in Tables 5 and 6, respectively.

Fig. 8 SEM micrographs of the a–d XY plane, a’–d’ XZ plane, and a’’–d’’ YZ plane of the PBF-LBed Ti6Al4V fabricated via a, b X scan and c, d XY scan strategy. The e, f are EDS analyses

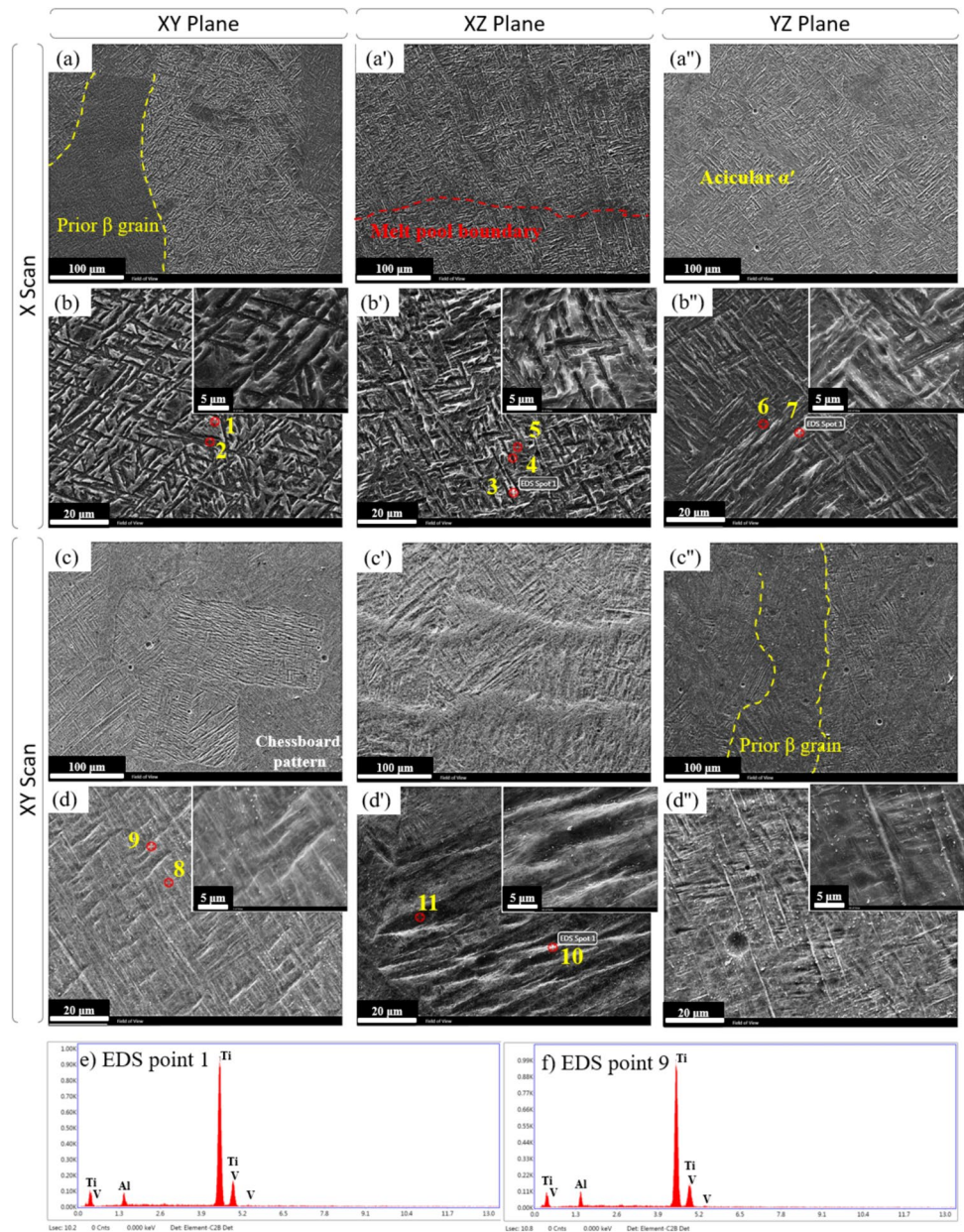


Table 4 Results of the EDS point analyses in Fig. 8

EDS (Points)	1	2	3	4	5	6	7	8	9	10	11
Elements (wt.%)											
Ti	92.0	91.5	90.4	92.7	92.8	89.9	91.1	91.8	91.0	93.2	92.3
Al	4.2	3.9	4.9	2.8	3.5	4.8	5.1	4.2	4.4	4.2	3.5
V	3.8	4.7	4.7	4.5	3.7	5.3	3.8	4.0	4.6	2.6	4.2

Despite using different corrosive environments, the PBF-LBed materials illustrated similar corrosion mechanisms. All of the tested materials presented a passive region after the active dissolution because of the formation of nonstoichiometric titanium oxide on the surface of the as-tested Ti6Al4V alloys [43]. However, due to the high concentration of the Cl⁻ contents in the diluted HCl solution (Fig. 12b),

corrosion occurs more severely as compared with the Ringer’s media (Fig. 12b). Therefore, the electrochemical properties of the PBF-LBed materials are more visible.

The X-scan PBF-LBed materials presented less corrosion resistance as compared with the XY-scan ones. The materials fabricated via the X scan strategy were manufactured with a higher laser energy density as compared with the XY

Fig. 9 Inverse pole figure (a–d), phase (a'–d'), and recrystallization (a''–d'') maps of PBF-LBed Ti6Al4V Samples via X scan (a, b) and XY scan (c, d) observed on XY plane (a, c) and YZ plane (b, d) with the corresponding pole figures

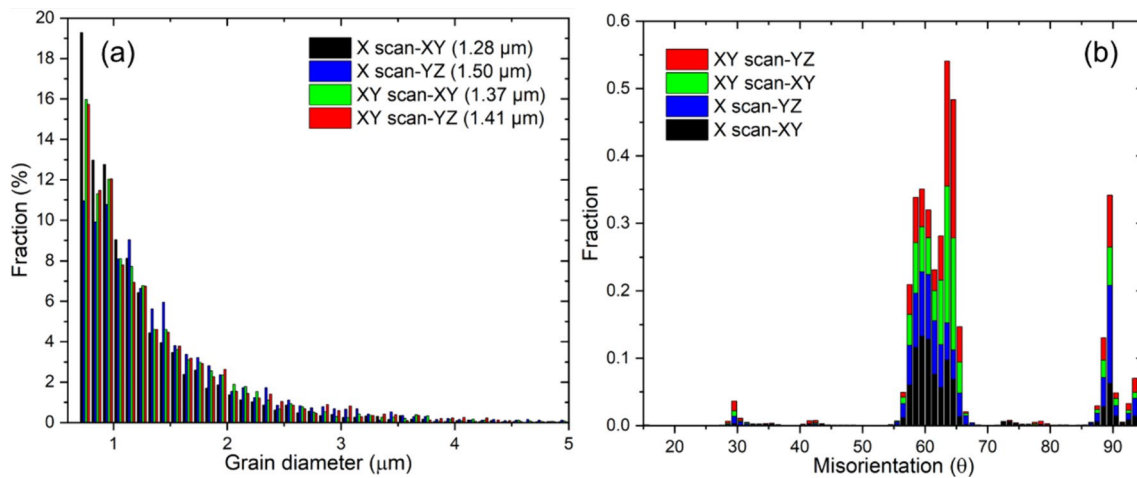
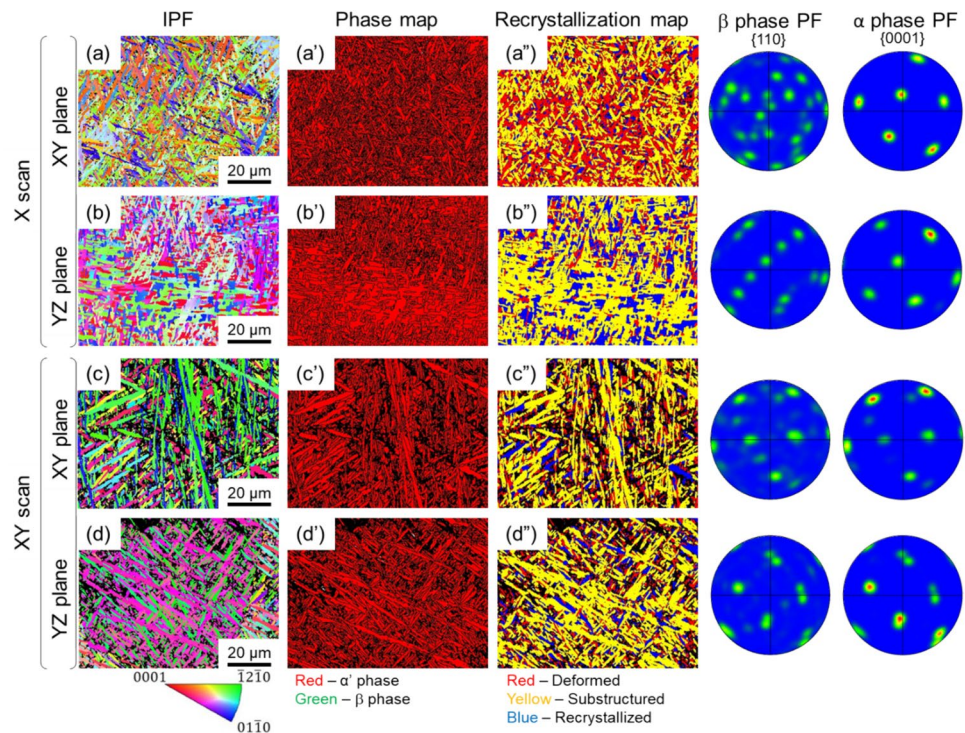


Fig. 10 Grain size distribution and grain boundary misorientation characteristics of PBF-LBed Ti6Al4V samples

scan ones; hence, they have more thermal stresses and more deformed grains. Also, according to the KAM values, the X-scan PBF-LBed materials have more kernel misorientation as compared with the XY-scan ones (Fig. 11).

The YZ planes of the both X-scan and XY-scan strategies illustrated superior corrosion properties as compared with the XY planes of the as-mentioned materials in both Ringer's and diluted HCl solutions. The YZ planes of both X-scan and XY-scan PBF-LBed samples had columnar structures; however, the XY planes illustrated more random grains. According to Fig. 9a, the deformed grains of the YZ

plane of the X-scan PBF-LBed sample were recrystallized and the fraction of the deformed grains was lower compared with the XY plane of the as-mentioned specimen; hence, the microstructure of the YZ plane of this material consisted of the substructure, recrystallized, and a low fraction of deformed grains. The YZ and the XY planes in the XY-scan PBF-LBed sample were almost the same. However, due to the more uniform microstructure of the YZ plane, more corrosion resistivity was presented. It should be mentioned that the amount of the β phase was under 1%, so, the effect

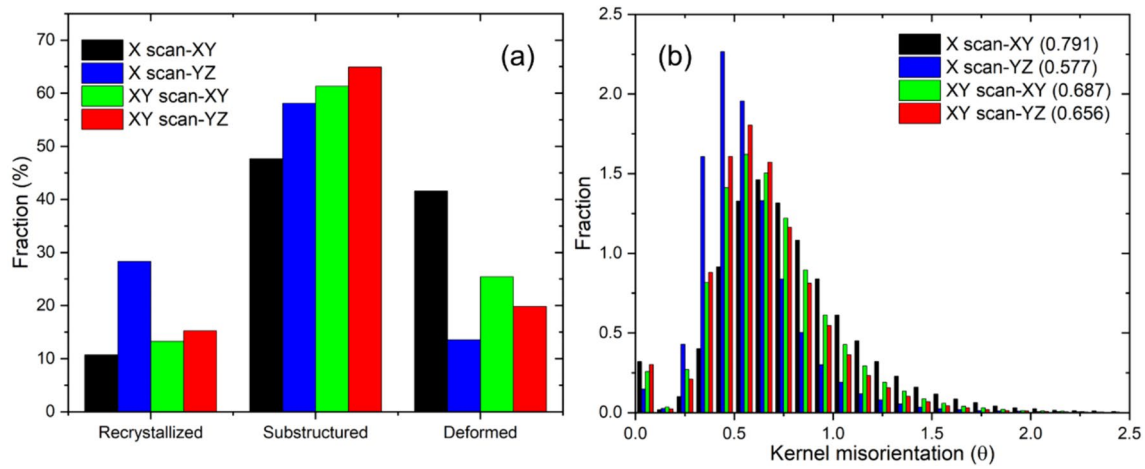


Fig. 11 Quantitative analysis of characteristics of grains and KAM values of PBF-LBed Ti6Al4V samples

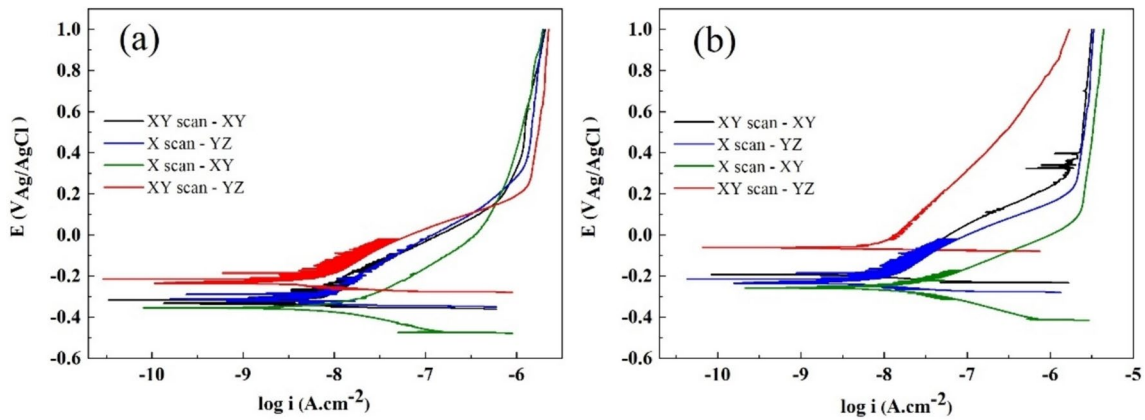


Fig. 12 Polarization curves of the fabricated specimens at **a** Ringer's as well as the **b** diluted HCl solutions, respectively

Table 5 Electrochemical behavior of the PBF-LBed Ti6Al4V samples in the Ringer's solution

Specimen	E_{corr} (V vs. Ag/AgCl)	i_{corr} (A cm ⁻²)	β_a (mV)	β_c (mV)
X scan—XY	-0.355	1.501×10^{-8}	0.279	0.082
X scan—YZ	-0.310	5.192×10^{-9}	0.243	0.016
XY scan—XY	-0.316	3.293×10^{-9}	0.210	0.010
XY scan—YZ	-0.215	2.766×10^{-9}	0.183	0.014

Table 6 Electrochemical behavior of the PBF-LBed Ti6Al4V samples in the diluted HCl solution

Specimen	E_{corr} (V vs. Ag/AgCl)	i_{corr} (A cm ⁻²)	β_a (mV)	β_c (mV)
X scan—XY	-0.258	2.109×10^{-8}	0.161	0.093
X scan—YZ	-0.215	8.706×10^{-9}	0.185	0.018
XY scan—XY	-0.193	8.778×10^{-9}	0.249	0.013
XY scan—YZ	-0.138	8.788×10^{-9}	0.378	0.006

of this phase on the corrosion properties of the PBF-LBed samples was negligible.

3.2.2 EIS measurements

EIS results of the PBF-LBed Ti6Al4V alloy were obtained after 60 min of immersion and stabilizing at OCP condition in both Ringer's agent and diluted HCl media. Nyquist, bode

phase, and equivalent electrical circuit of the aforementioned samples are presented in Fig. 13. Also, the results obtained from the EIS measurements from Ringer's solution and diluted HCl are listed in Tables 7 and 8, respectively; where R_{ct} is the charge transfer resistance, R_s is the solution resistance, and CPE is the constant phase element. It is noteworthy to mention that the measurements were repeated three times to ensure reproducibility. The equivalent electrical

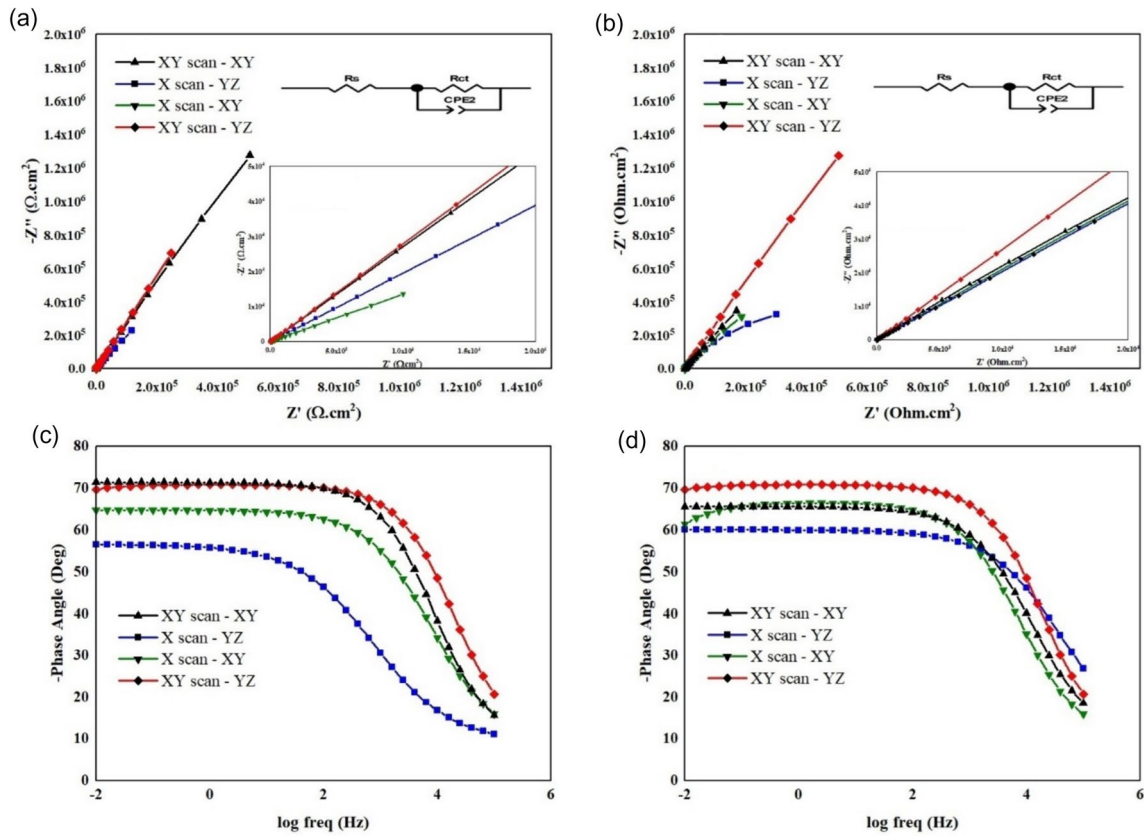


Fig. 13 Nyquist and Bode phase diagrams of PBF-LBed Ti6Al4V in **a** and **c** Ringer's solution, **b** and **d** diluted HCl solution, respectively

Table 7 EIS results of PBF-LBed Ti6Al4V samples in the Ringer's solution obtained from Fig. 13

Specimens	R _s (Ω cm ²)	CPE2		R _{ct} (Ω cm ²)
		C _{dl} (F cm ⁻²)	n ₂ (0-1)	
X scan—XY	17.536	6.187 × 10 ⁻⁵	0.77	8.229 × 10 ⁷
X scan—YZ	18.518	3.080 × 10 ⁻⁵	0.58	4.380 × 10 ¹²
XY scan—XY	17.006	1.182 × 10 ⁻⁵	0.78	1.982 × 10 ¹³
XY scan—YZ	17.985	2.682 × 10 ⁻⁵	0.69	5.574 × 10 ¹³

Table 8 EIS results of PBF-LBed Ti6Al4V samples in the diluted HCl solution obtained from Fig. 13

Specimens	R _s (Ω cm ²)	CPE2		R _{ct} (Ω cm ²)
		C _{dl} (F cm ⁻²)	n ₂ (0-1)	
X scan—XY	20.017	1.402 × 10 ⁻⁵	0.74	1.226 × 10 ⁶
X scan—YZ	20.809	1.929 × 10 ⁻⁵	0.72	3.213 × 10 ⁶
XY scan—XY	19.341	6.158 × 10 ⁻⁶	0.77	5.537 × 10 ⁷
XY scan—YZ	18.116	1.848 × 10 ⁻⁵	0.71	4.465 × 10 ⁹

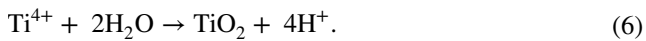
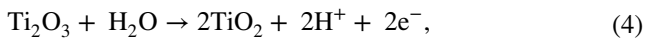
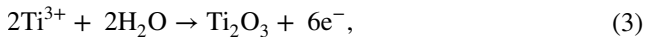
circuit consisted of CPE to more accurately fit the parameters. According to Toma et al. [44] due to the surface inhomogeneity and deviations from ideal dielectric behavior, the CPE parameter is being used to obtain the capacitance value. The CPE impedance is defined by:

$$Z_{CPE} = [C(j\omega)^n]^{-1} \tag{1}$$

where Z_{CPE} is the CPE impedance (Ω cm⁻²), C is the capacitance of an ideal capacitor (1 rad s⁻¹), j = √-1, ω is the angular frequency (rad s⁻¹), and 0 < n < 1 which is related to surface roughness [45].

According to the Nyquist diagram, all of the PBF-LBed specimens in both media illustrated semicircular curves which were due to the thin oxide passive layer formation (Fig. 13a). Also, the high phase contents in a wide range of frequencies present the passivation behavior of the aforementioned samples (Fig. 13b). Passivation is a frequently observed and advantageous feature in Ti6Al4V alloys, leading to the formation of an oxide film on the alloy's surface, primarily composed of TiO₂, TiO, and Ti₂O₃. This oxide film acts as an inhibitor, significantly enhancing the alloy's resistance to corrosion. Additionally, oxides of alloying elements like Al₂O₃ and VO_x (from α or β phases)

can also contribute to the development of a protective passive film on the Ti6Al4V alloy. The formation of this passive film is described by specific chemical reactions [46]:



4 Conclusion

This study investigated the controlled microstructures and corrosion behavior of Ti6Al4V alloy fabricated through Laser Beam Powder Bed Fusion (PBF-LB) using simultaneous change of laser scanning strategy (X scan and XY scan) and hatch space (low and medium). The results showed significant differences in microstructural characteristics between these controlled microstructures, including the distribution of prior β grains, acicular α' martensite, melt pool boundaries, and the formation of a chessboard pattern. Furthermore, the analysis of grain size and grain characteristics demonstrated the influence of the implemented controlled microstructure approach and observation plane on the grain structure.

Corrosion investigations revealed that the PBF-LB materials displayed a passive region after active dissolution in both Ringer's and diluted HCl solutions. However, the materials produced via the X-scan strategy exhibited lower corrosion resistance compared to the XY scan materials. This difference in corrosion behavior was attributed to the higher thermal stresses and more deformed grains in the X scan samples, which was supported by the KAM values. Interestingly, the YZ planes of both X scan and XY scan strategies exhibited superior corrosion resistance compared to the XY planes. The columnar structure and more uniform microstructure of the YZ plane contributed to this improved corrosion resistance.

Electrochemical impedance spectroscopy (EIS) measurements provided further insights into the corrosion behavior, showing semicircular Nyquist curves and high impedance values at low frequencies, indicating the presence of a protective passive layer on the surface of the PBF-LB samples.

As the main practical implications of this study, the findings could guide other researchers and highlight the significance of the controlled microstructure approach via simultaneous change of laser scanning strategy and hatch space (laser energy density) in influencing the microstructure and corrosion properties of PBF-LB Ti6Al4V alloy. However, some limitations exist in the present study such as sample size and geometry, limited scan strategies, corrosive environment (not including proteins regarding dental implants), post-processing (like different surface finishing), and in vivo investigations which can be good topics for further research.

Acknowledgements This work has also been partially supported by Grants-in-Aid for Scientific Research (Grant Number: 23H00235) from the Japan Society for the Promotion of Science (JSPS) and CREST (Grant Number: JPMJCR2194) from the Japan Science and Technology Agency (JST).

Author contributions Tohid Rajabi: conceptualization, methodology, validation, formal analysis, investigation, data curation, writing—original draft. Hamid Reza Ghorbani: conceptualization, methodology, investigation, data curation, writing—original draft. Masoud Atapour: conceptualization, resources, writing—review and editing, supervision, project administration, funding acquisition. Ozkan Gokcekaya: conceptualization, methodology, validation, resources, writing—review and editing, funding acquisition. Takayoshi Nakano: conceptualization, investigation, data curation, funding acquisition.

Data availability Data available on request/reasonable request.

Declarations

Conflict of interest On behalf of all authors, the corresponding author states that there is no conflict of interest. The authors declare that they have no known competing financial interests or personal relationships that could have appeared to influence the work reported in this paper.

References

1. Mosallanejad MH, Niroumand B, Aversa A, Saboori A (2021) In-situ alloying in laser-based additive manufacturing processes: A critical review. *J Alloys Compd* 872:159567. <https://doi.org/10.1016/j.jallcom.2021.159567>
2. Kouhi M, de Souza Araújo IJ, Asa'ad F et al (2024) Recent advances in additive manufacturing of patient-specific devices for dental and maxillofacial rehabilitation. *Dent Mater* 40:700–715. <https://doi.org/10.1016/j.dental.2024.02.006>
3. Methani MM, Cesar PF, de Paula Miranda RB et al (2020) Additive manufacturing in dentistry: current technologies, clinical applications, and limitations. *Curr Oral Heal Rep* 7:327–334. <https://doi.org/10.1007/s40496-020-00288-w>
4. Mace A, Khullar P, Bouknight C, Gilbert JL (2022) Corrosion properties of low carbon CoCrMo and additively manufactured CoCr alloys for dental applications. *Dent Mater* 38:1184–1193. <https://doi.org/10.1016/j.dental.2022.06.021>
5. Nazir A, Gokcekaya O, Md Masum Billah K et al (2023) Multi-material additive manufacturing: a systematic review of design, properties, applications, challenges, and 3D printing of materials and cellular metamaterials. *Mater Des* 226:111661. <https://doi.org/10.1016/j.matdes.2023.111661>

6. Ikee N, Matsumi T, Ishimoto T et al (2021) Fabrication of Ti-alloy powder/solid composite with uniaxial anisotropy by introducing unidirectional honeycomb structure via electron beam powder bed fusion. *Crystals* 11:1074
7. Zhang X-Y, Fang G, Leefflang S et al (2018) Effect of subtransus heat treatment on the microstructure and mechanical properties of additively manufactured Ti-6Al-4V alloy. *J Alloys Compd* 735:1562–1575. <https://doi.org/10.1016/j.jallcom.2017.11.263>
8. Behjat A, Shamanian M, Taherizadeh A et al (2022) Enhanced surface properties and bioactivity of additively manufactured 316L stainless steel using different post-treatments. *Mater Today Proc* 70:188–194. <https://doi.org/10.1016/j.matpr.2022.09.019>
9. Atapour M, Sanaei S, Wei Z et al (2023) In vitro corrosion and biocompatibility behavior of CoCrMo alloy manufactured by laser powder bed fusion parallel and perpendicular to the build direction. *Electrochim Acta* 445:142059. <https://doi.org/10.1016/j.electacta.2023.142059>
10. Gokcekaya O, Ishimoto T, Todo T et al (2021) Influence of powder characteristics on densification via crystallographic texture formation: Pure tungsten prepared by laser powder bed fusion. *Addit Manuf Lett* 1:100016. <https://doi.org/10.1016/j.addlet.2021.100016>
11. Alipour S, Moridi A, Liou F, Emdadi A (2022) The trajectory of additively manufactured titanium alloys with superior mechanical properties and engineered microstructures. *Addit Manuf* 60:103245. <https://doi.org/10.1016/j.addma.2022.103245>
12. Huang C-C, Li M-J, Tsai P-I et al (2020) Novel design of additive manufactured hollow porous implants. *Dent Mater* 36:1437–1451. <https://doi.org/10.1016/j.dental.2020.08.011>
13. Kim J-H, Kim M-Y, Knowles JC et al (2020) Mechanophysical and biological properties of a 3D-printed titanium alloy for dental applications. *Dent Mater* 36:945–958. <https://doi.org/10.1016/j.dental.2020.04.027>
14. Chung I, Lee J, Li L et al (2023) A preclinical study comparing single- and double-root 3D-printed Ti-6Al-4V implants. *Sci Rep* 13:862. <https://doi.org/10.1038/s41598-023-27712-2>
15. Yang F, Chen C, Zhou Q et al (2017) Laser beam melting 3D printing of Ti6Al4V based porous structured dental implants: fabrication, biocompatibility analysis and photoelastic study. *Sci Rep* 7:45360. <https://doi.org/10.1038/srep45360>
16. Cohen DJ, Cheng A, Kahn A et al (2016) Novel osteogenic Ti-6Al-4V device for restoration of dental function in patients with large bone deficiencies: design, development and implementation. *Sci Rep* 6:20493. <https://doi.org/10.1038/srep20493>
17. Watanabe R, Matsugaki A, Gokcekaya O et al (2023) Host bone microstructure for enhanced resistance to bacterial infections. *Biomater Adv* 154:213633. <https://doi.org/10.1016/j.bioadv.2023.213633>
18. Bhargav A, Sanjairaj V, Rosa V et al (2018) Applications of additive manufacturing in dentistry: a review. *J Biomed Mater Res B Appl Biomater* 106:2058–2064. <https://doi.org/10.1002/jbm.b.33961>
19. Ng LL, Sing SL (2022) Additive manufacturing enabled designs for dental applications: a conceptual study. *Mater Today Proc* 70:548–553. <https://doi.org/10.1016/j.matpr.2022.09.556>
20. Zadeh MK, Yeganeh M, Shoushtari MT et al (2022) Microstructure, corrosion behavior, and biocompatibility of Ti-6Al-4V alloy fabricated by LPBF and EBM techniques. *Mater Today Commun* 31:103502. <https://doi.org/10.1016/j.mtcomm.2022.103502>
21. Lu H, Deng W, Luo K et al (2023) Tailoring microstructure of additively manufactured Ti6Al4V titanium alloy using hybrid additive manufacturing technology. *Addit Manuf* 63:103416. <https://doi.org/10.1016/j.addma.2023.103416>
22. Ghorbani HR, Mosallanejad MH, Atapour M et al (2022) Hybrid additive manufacturing of an electron beam powder bed fused Ti6Al4V by transient liquid phase bonding. *J Mater Res Technol* 20:180–194. <https://doi.org/10.1016/j.jmrt.2022.07.009>
23. Aufa AN, Hassan MZ, Ismail Z (2022) Recent advances in Ti-6Al-4V additively manufactured by selective laser melting for biomedical implants: prospect development. *J Alloys Compd* 896:163072. <https://doi.org/10.1016/j.jallcom.2021.163072>
24. Aufa AN, Hassan MZ, Ismail Z et al (2022) Surface enhancement of Ti-6Al-4V fabricated by selective laser melting on bone-like apatite formation. *J Mater Res Technol* 19:4018–4030. <https://doi.org/10.1016/j.jmrt.2022.06.135>
25. Sichani HR, Atapour M, Ashrafizadeh F et al (2024) Mechanical, electrochemical and permeability behaviour of Ti6Al-4V scaffolds fabricated by electron beam powder bed fusion for orthopedic implant applications: The role of cell type and cell size. *J Mater Res Technol* 28:3240–3257. <https://doi.org/10.1016/j.jmrt.2023.12.260>
26. Barba D, Alabort C, Tang YT et al (2020) On the size and orientation effect in additive manufactured Ti-6Al-4V. *Mater Des* 186:108235. <https://doi.org/10.1016/j.matdes.2019.108235>
27. Yang J, Yu H, Yin J et al (2016) Formation and control of martensite in Ti-6Al-4V alloy produced by selective laser melting. *Mater Des* 108:308–318. <https://doi.org/10.1016/j.matdes.2016.06.117>
28. Ekubaru Y, Gokcekaya O, Ishimoto T et al (2022) Excellent strength–ductility balance of Sc-Zr-modified Al–Mg alloy by tuning bimodal microstructure via hatch spacing in laser powder bed fusion. *Mater Des* 221:110976. <https://doi.org/10.1016/j.matdes.2022.110976>
29. Cao S, Zou Y, Lim CVS, Wu X (2021) Review of laser powder bed fusion (LPBF) fabricated Ti-6Al-4V: process, post-process treatment, microstructure, and property. *Light Adv Manuf* 2:313–332. <https://doi.org/10.37188/lam.2021.020>
30. Simonelli M, Tse YY, Tuck C (2014) On the texture formation of selective laser melted Ti-6Al-4V. *Metall Mater Trans A* 45:2863–2872. <https://doi.org/10.1007/s11661-014-2218-0>
31. Elsayed M, Ghazy M, Youssef Y, Essa K (2019) Optimization of SLM process parameters for Ti6Al4V medical implants. *Rapid Prototyp J* 25:433–447. <https://doi.org/10.1108/RPJ-05-2018-0112>
32. Cabrini M, Carrozza A, Lorenzi S et al (2022) Influence of surface finishing and heat treatments on the corrosion resistance of LPBF-produced Ti-6Al-4V alloy for biomedical applications. *J Mater Process Technol* 308:117730. <https://doi.org/10.1016/j.jmatprotec.2022.117730>
33. Toptan F, Alves AC, Carvalho Ó et al (2019) Corrosion and tribo-corrosion behaviour of Ti6Al4V produced by selective laser melting and hot pressing in comparison with the commercial alloy. *J Mater Process Technol* 266:239–245. <https://doi.org/10.1016/j.jmatprotec.2018.11.008>
34. Xiang S, Yuan Y, Zhang C, Chen J (2022) Effects of process parameters on the corrosion resistance and biocompatibility of Ti6Al4V parts fabricated by selective laser melting. *ACS Omega* 7:5954–5961. <https://doi.org/10.1021/acsomega.1c06246>
35. Leban MB, Kosec T, Finšgar M (2022) Corrosion characterization and ion release in SLM-manufactured and wrought Ti6Al4V alloy in an oral environment. *Corros Sci* 209:110716. <https://doi.org/10.1016/j.corsci.2022.110716>
36. Liu J, Li G, Sun Q et al (2022) Understanding the effect of scanning strategies on the microstructure and crystallographic texture of Ti-6Al-4V alloy manufactured by laser powder bed fusion. *J Mater Process Technol* 299:117366. <https://doi.org/10.1016/j.jmatprotec.2021.117366>
37. Mosallanejad MH, Sanaei S, Atapour M et al (2022) Microstructure and corrosion properties of CP-Ti processed by laser powder bed fusion under similar energy densities. *Acta Metall Sin (Engl Lett)* 35:1453–1464. <https://doi.org/10.1007/s40195-022-01376-9>

38. Keller T, Lindwall G, Ghosh S et al (2017) Application of finite element, phase-field, and CALPHAD-based methods to additive manufacturing of Ni-based superalloys. *Acta Mater* 139:244–253. <https://doi.org/10.1016/j.actamat.2017.05.003>
39. Kazantseva N, Krakhmalev P, Thuvander M et al (2018) Martensitic transformations in Ti-6Al-4V (ELI) alloy manufactured by 3D Printing. *Mater Charact* 146:101–112. <https://doi.org/10.1016/j.matchar.2018.09.042>
40. Kamath RR, Nandwana P, Ren Y, Choo H (2021) Solidification texture, variant selection, and phase fraction in a spot-melt electron-beam powder bed fusion processed Ti-6Al-4V. *Addit Manuf* 46:102136. <https://doi.org/10.1016/j.addma.2021.102136>
41. Ekubaru Y, Gokcekaya O, Nakano T (2022) Effects of scanning strategy on the microstructure and mechanical properties of Sc-Zr-modified Al–Mg alloy manufactured by laser powder bed fusion. *Crystals* 12:1348
42. Kamaya M, Wilkinson AJ, Titchmarsh JM (2006) Quantification of plastic strain of stainless steel and nickel alloy by electron backscatter diffraction. *Acta Mater* 54:539–548. <https://doi.org/10.1016/j.actamat.2005.08.046>
43. Pohrelyuk IM, Fedirko VM, Tkachuk OV, Proskurnyak RV (2013) Corrosion resistance of Ti–6Al–4V alloy with nitride coatings in Ringer's solution. *Corros Sci* 66:392–398. <https://doi.org/10.1016/j.corsci.2012.10.005>
44. Toma O, Rotella H, Dahab H et al (2021) Tysonite-type solid state electrolyte for fluoride ion batteries: highly dense thin film by PVD processing. *J Alloys Compd* 862:158683. <https://doi.org/10.1016/j.jallcom.2021.158683>
45. Rajabi T, Atapour M, Elmkhah H, Nahvi SM (2022) Nanometric CrN/CrAlN and CrN/ZrN multilayer physical vapor deposited coatings on 316L stainless steel as bipolar plate for proton exchange membrane fuel cells. *Thin Solid Films* 753:139288. <https://doi.org/10.1016/j.tsf.2022.139288>
46. Mahlobo MGR, Chikosha L, Olubambi PA (2022) Study of the corrosion properties of powder rolled Ti–6Al–4V alloy applied in the biomedical implants. *J Mater Res Technol* 18:3631–3639. <https://doi.org/10.1016/j.jmrt.2022.04.004>

Publisher's Note Springer Nature remains neutral with regard to jurisdictional claims in published maps and institutional affiliations.

Springer Nature or its licensor (e.g. a society or other partner) holds exclusive rights to this article under a publishing agreement with the author(s) or other rightsholder(s); author self-archiving of the accepted manuscript version of this article is solely governed by the terms of such publishing agreement and applicable law.